THE JOURNAL OF PHYSICAL CHEMISTRY C
A JOURNAL OF THE AMERICAN CHEMICAL SOCIETY

pubs.acs.org/JPCC
Article

Temperature-Dependent Transient Photocurrent Investigations for 2D, 3D, and Hybrid 2D/3D Tin Perovskite Films

Ashank Seetharaman, Sudhakar Narra, Parameswaran Rajamanickam, Nobuhiro Ohta, and Eric Wei-Guang Diau*

Cite This: J. Phys. Chem. C 2025, 129, 18563−18570

ABSTRACT: Understanding the interplay between electronic and ionic dynamics in tin halide perovskites is critical for optimizing their photovoltaic performance and stability. Here, we combine temperature-dependent transient photocurrent (TPC) and photoluminescence (PL) measurements under a lateral bias in a coplanar-electrode geometry for a 2D Dion−Jacobson phase (B1: $BDASnI_4$), a 3D phase (E1: $FASnI_3$), and their physically paired 2D/3D hybrid (E1B1) phase. In B1, rapid carrier extraction ($\tau_{rise} \sim 1$ ms) and a pronounced PL red-shift (−0.8 meV/K) reflect strong electron−phonon coupling and minimal ionic screening. Arrhenius analysis of I_{ph} reveals two activation energies, $E_a \sim 0.13$ eV at low temperature T and a higher barrier of ∼1.4 eV above ∼320 K, indicating the emergence of deeply bound trap populations. The 3D E1 exhibits sluggish kinetics ($\tau_{rise} \sim 90$ ms), a +0.6 meV/K blue-shift, and three activation regimes ($E_a \sim 0.34$, 0.50, and 0.70 eV), consistent with migrating iodide vacancies. The E1B1 hybrid film shows dual PL emissions and a trifurcated activation profile ($E_a \sim 0.24$, 0.43, and 0.63 eV), capturing interfacial passivation at low T and trap-dominated ionic pinning at high T. By correlating spectral shifts with TPC-derived energetics, we demonstrate how dimensionality and interfacial chemistry together dictate exciton behavior, ionic mobility, and thermal response under device operational conditions.

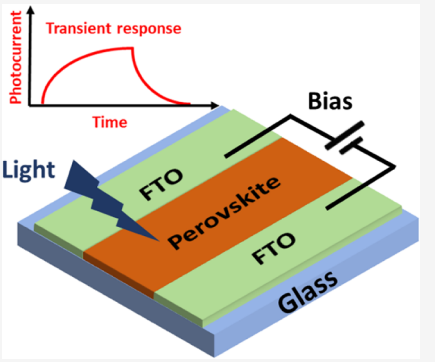

1. INTRODUCTION

Lead (Pb) halide perovskites have attracted intense attention for optoelectronic applications due to their high absorption coefficients,[1] long diffusion lengths,[2] and excellent defect tolerance,[3,4] enabling high-performance solar cells.[5−8] However, the inherent toxicity of lead hinders its commercial viability. As a sustainable alternative, tin (Sn)-based halide perovskites, particularly formamidinium-based tin iodide ($FASnI_3$) perovskites, have emerged as lead-free analogs that retain many beneficial characteristics, including a direct bandgap near 1.4 eV and strong light absorption.[9−16] Nevertheless, they suffer from intrinsic problems, in particular, $Sn^{2+} \rightarrow Sn^{4+}$ oxidation in which tin perovskite films tend to crystallize very rapidly, yielding small grains, high defect densities, and inducing p-type self-doping.[17−20]

Structural engineering via 2D/3D hybrid architectures has proven to be effective at mitigating these issues. In such systems, thin 2D layers cap the 3D bulk, while organic spacers chemically passivate the surface, and grain-boundary defects, simultaneously acting as hydrophobic barriers to moisture ingress. The strong bonding between the spacer cations and the 3D lattice promotes more uniform crystallization of the underlying framework, resulting in improved film quality, reduced trap density, and enhanced photovoltaic (PV) performance.[21−23] Notably, phenethylammonium (PEA^+) incorporation into triple halide-based 3D Sn perovskite has achieved record efficiencies of 17.13% by improving crystallinity and inducing favorable out of plane orientation.[24] Other notable works which focused on improving the crystallinity of 3D bulk leading to high efficiencies have also been demonstrated using related 2D/3D hybrid strategies.[25−30] Although 2D/3D hybrids are typically formed either by sequential deposition of spacer cations onto a 3D lattice[31] or by incorporating spacers directly into the 3D precursor, an alternative "physical coupling" approach has emerged. In our previous work, we showed that placing a separate 2D film in physical contact with $FASnI_3$ drives the migration of butylammonium (BA^+), hexylammonium (HA^+), and octylammonium (OA^+) spacers into the 3D lattice, forming interfacial quasi-2D domains.[32] Similarly, Mathew et al. also have shown that cation migration between 2D and 3D layers can induce phase transitions with activation energies of 29−50 kJ/mol, by physical pairing.[33] Along similar lines, halide ion exchange in physically paired films was also explored.[34,35] This physical-contact strategy was also extended to Pb-

Received: July 27, 2025
Revised: September 25, 2025
Accepted: September 26, 2025
Published: October 2, 2025

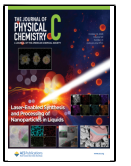

https://doi.org/10.1021/acs.jpcc.5c05203
J. Phys. Chem. C 2025, 129, 18563−18570

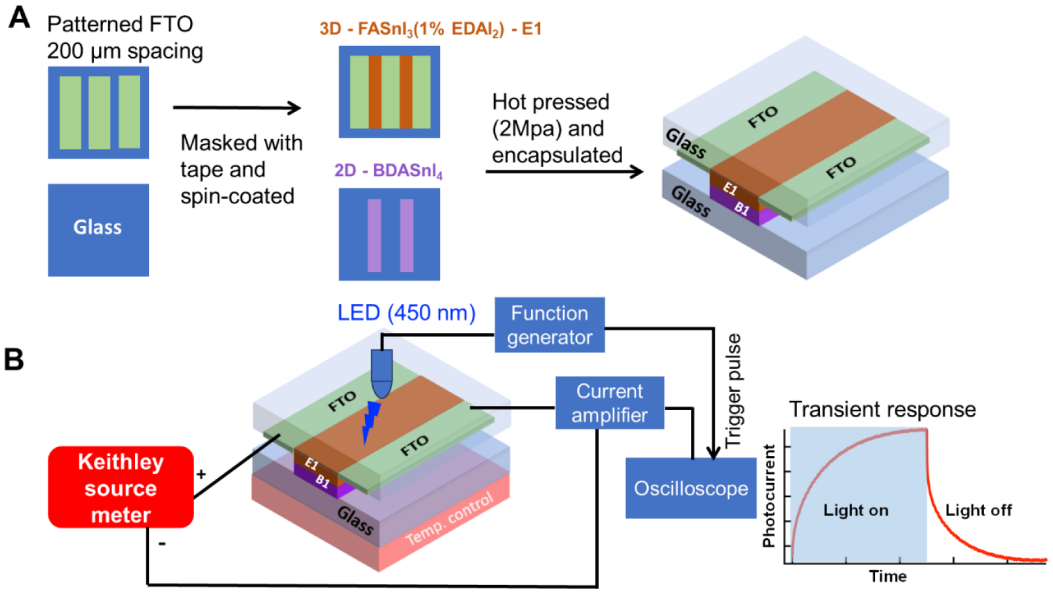

Figure 1. Physically stacked 2D/3D tin perovskite hybrid structure on coplanar electrodes and experimental setup for transient photocurrent (TPC) measurement. (A) Schematic illustration of the sample preparation process on patterned FTO. The samples are then hot pressed together under 2 MPa pressure and encapsulated to form a 2D/3D hybrid. (B) The TPC response is recorded through a current amplifier by the impinging pulsed LED light (driven by a function generator) on pristine (B1 and E1) as well as 2D/3D hybrid samples, which are externally biased by a source meter.

perovskites: hot-pressing a 2D layer onto a 3D film under high pressure produced a 2D/3D hybrid device with a record efficiency of 24.35%.[36] These results underscore the intrinsic "softness" of the 3D lattice, whose chemical composition and phase behavior can be readily tuned by simple physical contact. Underlying this softness is facile ion migration: mobile vacancies and cations freely traverse the bulk dynamically screening applied fields and inducing hysteresis.[37−39] Consequently, understanding ion migration is critical for diagnosing and mitigating its detrimental impact on PV performance.[40−42] While many studies infer ionic behavior indirectly, systematic quantification of ionic relaxation time scales remains scarce. Transient photocurrent (TPC) measurements address this gap by probing coupled carrier-ion kinetics under pulsed light and bias.[43−45] In 3D Pb-perovskites, TPC reveals an initial current spike from interfacial band-bending modifications, followed by slow transients dominated by ion migration. Using this technique, bulk ion migration activation energies (0.34−0.67 eV) are extracted from temperature-dependent signal decay, distinguishing electronic traps in 2D perovskites from ionic effects in 3D systems.[46] This methodology has since been applied across a variety of perovskite compositions to elucidate their coupled electronic−ionic behavior.[47−49] TPC studies on Sn-based analogs have likewise been reported, but these primarily focused on device performance metrics rather than a detailed analysis of ionic relaxation.[50−53]

To address this gap, we performed comprehensive TPC measurements on tin perovskites—specifically on 2D $BDASnI_4$ (B1, 1,4-butanediammonium tin iodide), 3D $FASnI_3$ (E1 with 1% $EDAI_2$), and their 2D/3D hybrid (E1B1). The hybrid films were created by physically pairing separate 2D and 3D layers, enabling the direct investigation of interfacial interactions. Dion-Jacobson (DJ) perovskites were specifically chosen for their superior structural rigidity compared to Ruddlesden−Popper (RP) analogues, arising from a single layer of diammonium cations forming strong hydrogen bonds and electrostatic interactions with the inorganic slabs, rather than the weaker van der Waals gap inherent in RP structures.[54] While DJ layers are often used to suppress uncontrolled ion migration, their true utility here lies in their ability to modulate—but not entirely block—vacancy motion, making them ideal for studying interfacial dynamics. By comparing the TPC responses of pristine 2D, 3D, and physically paired 2D/3D films, we can directly probe how the DJ overlayer alters vacancy transport, field screening, and trap formation within the underlying 3D perovskite. To correlate these electrical dynamics with band-structure modulation, we performed photoluminescence (PL) excitation between biased electrodes, directly probing electric-field-modulated emission under operational conditions. This simultaneous application of TPC and PL under identical bias rarely combined even for Pb-based perovskites[55] enables us to establish a direct connection between ion migration dynamics and interfacial band-structure evolution in Sn perovskites. Together, our combined TPC and PL studies demonstrate that DJ-type 2D layers can suppress ionic screening and enable rapid carrier extraction, while pure 3D tin perovskites exhibit high ionic barriers and sluggish dynamics and that physically paired 2D/3D interfaces uniquely mediate these extremes through temperature-dependent trap formation and lattice relaxation.

2. METHODS

2.1. Device Preparation and Characterization. The samples comprised 2D, 3D, and physically paired 2D/3D hybrid Sn-based perovskites deposited on fluorine-doped tin oxide (FTO) substrates configured in a lateral coplanar electrode geometry with a 200 μm gap (patterning methods are detailed in Supporting Information), as schematized in Figure 1A. Electrical contacts were applied to the coplanar electrodes for TPC and PL measurements under bias. The 2D DJ-type perovskite samples include B1 ($BDASnI_4$), while the

https://doi.org/10.1021/acs.jpcc.5c05203
J. Phys. Chem. C 2025, 129, 18563−18570

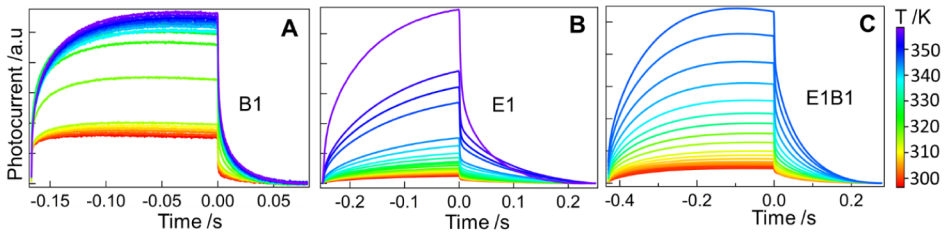

Figure 2. Transient photocurrent (TPC) spectra of 2D, 3D, and physically stacked 2D/3D tin hybrid structures on coplanar electrodes under −2.5 V external bias and 450 nm LED excitation at different temperatures ranging from ∼296 to 358 K for (A) B1, (B) E1, and (C) E1B1.

3D perovskite sample (E1) was composed of $FASnI_3$ doped with 1% ethylenediammonium diiodide ($EDAI_2$). Full experimental procedures for pristine film preparation, as well as structural and photophysical characterization, are provided in the Supporting information. Additionally, physically coupled 2D/3D hybrids, E1B1, were fabricated by stacking the 2D layer (spin-coated on glass) atop the E1 3D perovskite under 2 MPa pressure using a hot press machine, followed by encapsulation.

The X-ray diffraction (XRD) patterns, scanning electron micrograph (SEM), UV−Vis, and photoluminescence (PL) spectra of the pristine samples are shown in Figures S2−S5. The structural and optical characteristics of our 2D DJ-type perovskite (B1) agree well with previous reports.[56,57] XRD shows an intense (00l) peak ($\theta < 10°$ for both B1) indicative of a well-ordered layered structure, while SEM images reveal smooth, plate-like morphologies of 2D films (Figures S2 and S3). In the UV−Vis spectra (Figure S4), a pronounced excitonic absorption feature appears near 600 nm, further confirming the formation of a quantum-well-type layered perovskite structure. The PL spectra (Figure S5) of the 2D $BDASnI_4$ (B1) lattice shows its excitonic maximum at ∼610 nm while that of the pure 3D $FASnI_3$ (E1) film exhibits a band-edge emission peak centered at ∼890 nm.

2.2. Transient Photocurrent Measurement. For TPC characterization, samples were excited by using a 450 nm light source modulated by a function generator, providing periodic illumination synchronized with the detection system. The resulting photocurrent response from the perovskite devices was amplified by using a low-noise current amplifier and captured by using a digital oscilloscope, ensuring high-resolution temporal tracking of both the photocurrent rise and decay components. To investigate the temperature-dependent behavior of charge transport and ionic migration, a polyimide heater equipped with a closed-loop thermostat was employed, allowing precise and stable control of the sample temperature within the range of ∼23 to 85 °C (∼296 K to 358 K). The full experimental circuit including the pulsed light source, current amplifier, and oscilloscope is schematically represented in Figure 1B.

TPC was measured under an applied bias of −2.5 V across the coplanar electrodes. This bias voltage was optimized to achieve a sufficient signal-to-noise ratio in photocurrent measurements, ensuring effective carrier drift across the 200 μm channel for robust signal detection. PL was also carried out in a similar lateral electrode configuration with laser excitation on the perovskite layer (instrumentation details are given in the Supporting information).

3. RESULTS AND DISCUSSION

3.1. Transient Photocurrent (TPC) Dynamics in Sn-Based Perovskite Systems. The temperature-dependent TPC dynamics of B1, E1, and E1B1 Sn perovskites are shown in Figure 2A−C. They show an initial rise, stabilization, and decay of the photocurrent following slow pulsed excitation. These dynamics stem from the complex interaction between photogenerated charge carriers and the motion of mobile ionic species. When a lateral electric field is applied across coplanar electrodes, and the sample is illuminated, photogenerated electrons and holes quickly separate and drift toward the collecting electrodes, producing the initial rise and stabilization of the photocurrent in the observed TPC decay profiles. In contrast, once the light is switched off, the photocurrent gradually decays according to the diffusivity of the remaining charge carriers generated in the films during photoirradiation.

However, Sn perovskites, known for their soft lattices, have mobile defects that migrate under the electric field and temperature, altering the internal field and influencing the TPC profiles further. These ionic species migrate on time scales ranging from hundreds of microseconds to several milliseconds reflecting on photocurrent.[39,58] As carriers drift, many are temporarily captured by shallow or deep electronic trap states at grain boundaries, surfaces, and structural defects, especially in 3D systems like $FASnI_3$. These traps must be filled before efficient extraction occurs. Efficient charge extraction occurs only after these traps are filled, causing the photocurrent to rise gradually. Thus, the rise time (τ_{rise}) reflects both intrinsic carrier drift and the time required to saturate the available trap states. Concurrently, mobile ion (e.g., Sn and iodide vacancies) redistribution screens the internal field and shapes the TPC signal further.

Similarly, the decay phase is also influenced not only by diffusivity but also by defect-mediated processes. Typically, TPC decays follow a characteristic biexponential decay behavior, indicating two distinct but coupled relaxation processes.[39,59−61] The initial, faster decay component (τ_1 on the order of 0.2−6 ms) corresponds to the rapid recombination of free carriers and the depopulation of shallow trap states (due to Sn vacancies), whereas slow decay arises (τ_2 on the order of 11−120 ms) from deeper trap states caused by the ion migration due to illumination. The full temperature-dependent plots of both τ_1 and τ_2 across our B1, E1, and E1B1 samples are shown in Figures S6 and S7, respectively. To reduce the complexity in the discussion, we focused on the rise time as a metric that reports on trap-filling dynamics for comparative analysis. Full fitting parameters for both rise and decay components are provided in Tables S1−S3.

The temperature dependences of the photocurrent rise and amplitude of B1, E1, and E1B1 are shown in Figure 3A,B, respectively. The photocurrent rise times (Figure 3A) for Sn perovskite samples show a drastic change from B1 (2D) to E1 (3D), and the E1B1 (2D/3D) hybrid shows rise times in between those two samples at higher temperatures. The

https://doi.org/10.1021/acs.jpcc.5c05203
J. Phys. Chem. C 2025, 129, 18563−18570

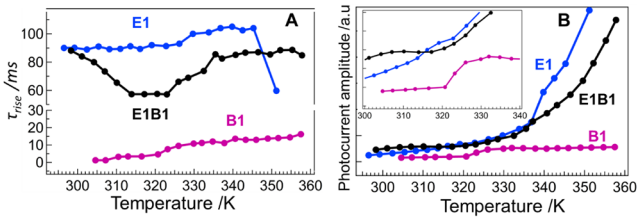

Figure 3. (A) Distribution of τ_{rise} obtained by fitting TPC profiles given in Figure 2 at different temperatures ranging from ∼296 to 358 K for B1, E1, and E1B1 and (B) magnitude of transient photocurrent (TPC) amplitudes I_{ph} for B1, E1, and E1B1 from ∼296 to 358 K.

differences in the rise times between B1 and E1 stem from the difference in the carrier mobilities and defect densities between the samples. The faster rise time of B1 can be attributed to the excellent long-range (in-plane) mobility in 2D perovskites over 3D perovskites.[62] However, confinement effects of 2D perovskites lead to inefficient carrier splitting, leading to smaller photocurrents compared to 3D perovskites (Figure 3B). E1 and E1B1 (3D and quasi-3D) samples displayed higher photocurrents compared to B1 (2D) at all temperatures for the aforementioned reason. Further, the improvement in the photocurrent in the E1B1 sample compared to E1 is due to the passivation effects of B1 on E1 in the 2D/3D hybrid samples. Additionally, high densities of Sn vacancies (∼10^{15} cm^{-3} vs ∼10^{10} cm^{-3} for Pb perovskites)[28,63] and mobile iodide defects enhance ionic screening effects, delaying the establishment of the internal electric field required for efficient carrier drift, which leads to the slower rise of photocurrent in 3D (E1) and 2D/3D (E1B1) Sn perovskites.

The photocurrent rise time (τ_{rise}) of B1 showed a gradual increment from 1.2 to 16 ms with an increase of temperature from room temperature (RT) to 360 K. Similarly, E1 also shows a gradual increase of τ_{rise} values; however, these changes are modest (±10 ms) compared to the observed rise time of 90 ms at room temperature. However, a significant drop was observed at 351 K. The gradual increase of τ_{rise} values for B1 and E1 with temperature can be attributed to suppressed carrier mobilities and concurrent thermal activation of defects,[64] whereas the observed drastic change in τ_{rise} at 351 K for E1 could be due to variation in the defect profile. Interestingly, the E1B1 sample showed a change in τ_{rise} with a decrease in value from 88 to 66 ms for the temperature range between 298 and 326 K, and then gradually increases to 85 ms up to 358 K.

The distinct trend observed for the τ_{rise} in the hybrid E1B1 system can be explained based on two coupled interfacial effects arising from the physical pairing of the 2D cap (B1) with the 3D bulk (E1): (i) passivating interaction at the 2D/3D boundary that neutralizes surface Sn-related traps and reduces interfacial recombination sites and (ii) thermally assisted ion exchange that nucleates quasi-n = 2 domains at the contact, producing a low-energy pathway for carrier extraction. As a result of these effects, τ_{rise} in E1B1 initially decreases with temperature up to ∼323 K. Above ∼326 K, thermal activation destabilizes the interface: enhanced ionic motion and thermally driven structural mismatch promote the formation of new interfacial defects and deeper trap states. These thermally activated traps increase the carrier capture cross-section and require additional trap-filling before steady extraction can occur, thus lengthening τ_{rise}. The net result is a temperature window in which the 2D cap first improves extraction and then at higher temperatures contributes to trap-limited kinetics as the interfacial landscape evolves. The physical contact interaction between the 2D and 3D Sn-perovskite films has been well documented.[32]

Temperature-dependent PL experiments were conducted to probe the electronic structure changes in B1, E1, and E1B1 that lead to the observed TPC dynamics (Figure 4). The E1B1 samples were illuminated on the E1 side as we are interested in understanding the effects of B1 on E1 under external stimulus. The PL intensities of B1, E1, and E1B1 (Figure 4A–C) decrease from ∼296 K to 358 K due to thermally activated nonradiative recombination, primarily driven by Sn^{4+} defect formation.[65] In addition to the decrease of PL intensities, these samples also demonstrate shifts in the PL peak maxima. The E1 side of the E1B1 sample showed emission from n = 2 at 700 nm in addition to the emission peak from the native E1 state at 870 nm. These observations are in line with the electronic structure changes in the physically stacked films discussed in the previous works.[32] Further, the dilations in the band gaps were fitted to obtain temperature coefficients that can be correlated to electron–phonon (EP) coupling.[66]

B1 shows a negative temperature coefficient of −0.8 ± 0.1 meV/K (Figure 4D), indicative of strong EP coupling,[67] and the thermal vibrations in the confined 2D lattice reduced the Sn–I orbital overlap, which led to a reduction in the

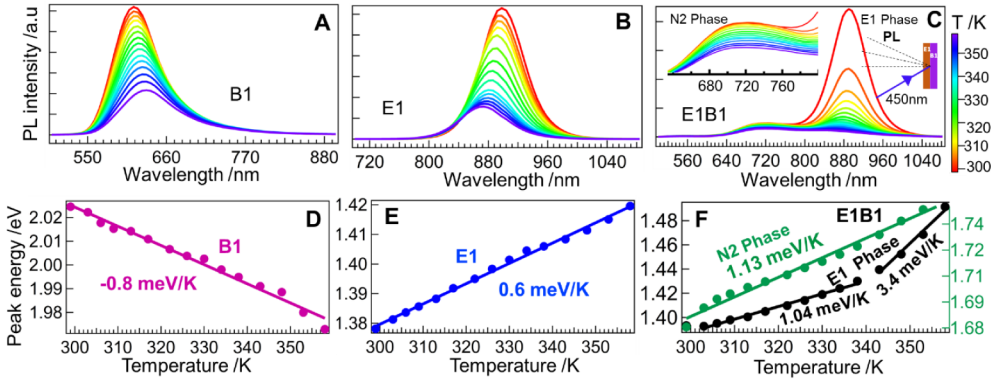

Figure 4. Photoluminescence (PL) spectra of 2D, 3D, and physically stacked 2D/3D hybrid structures on coplanar electrodes under −2.5 V external bias and 450 nm excitation wavelength at different temperatures ranging from ∼296 to 358 K for (A) B1, (B) E1, and (C) E1B1 and a plot of peak energy vs temperature extracted from temperature-dependent PL spectra for (D) B1, (E) E1, and (F) E1B1. The E1B1 sample exhibits two emitting phases—quasi-2D N2 and E1, and the E1 phase displays two distinct temperature coefficients.

https://doi.org/10.1021/acs.jpcc.5c05203
J. Phys. Chem. C 2025, 129, 18563−18570

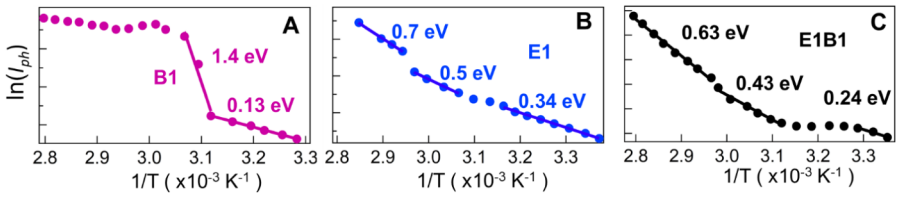

Figure 5. Activation energy E_a derived from the photocurrent amplitude I_{ph} for (A) B1, (B) E1, and (C) E1B1. All three samples exhibit distinct activation regimes reflecting the temperature-dependent evolution of trap states.

bandgap. In contrast, E1 shows a positive temperature coefficient of +0.6 ± 0.1 meV/K (Figure 4E), consistent with thermal expansion-induced widening of the bandgap. Elongation of Sn−I bonds weakens antibonding interactions, raising the conduction band edge.

The physically paired E1B1 hybrid showed complex temperature effects due to dimensional coexistence and interfacial interactions. The quasi-2D ($n \sim 2$) peak displayed a positive temperature coefficient of +1.13 ± 0.1 meV/K, characteristic of thermal expansion in partially confined domains (Figure 4F) whereas the E1-like peak in the hybrid showed two distinct positive temperature coefficients of +1.04 ± 0.1 meV/K (for ∼300−340 K range) and +3.4 ± 0.1 meV/K (above 340 K), reflecting interfacial strain-induced bandgap expansion. The temperature effects of PL agree well with the change in dynamics of the TPC rise dynamics for E1B1 hybrids at higher temperatures.

The energy barriers associated with net charge extraction (i.e., activation energies (E_a)) were sought from the temperature dependence of photocurrent amplitudes (I_{ph}) using the Arrhenius-type relationship: $I_{ph} \propto \exp(-E_a/kT)$, where k is the Boltzmann constant and T is the absolute temperature. This approach captures the cumulative thermal barrier associated with charge extraction, encompassing the combined effects of trap-assisted recombination, ionic migration, and lattice relaxation under applied bias. Compared to lifetime-based (τ) fittings, which often deviate from Arrhenius behavior due to overlapping carrier relaxation and ionic redistribution processes, the photocurrent amplitude provides a more integrated measure of transport-limiting processes. The extracted E_a values (Figure 5A−C) reveal distinct thermally activated regimes that correlate with the lattice dimensionality and defect chemistry across the Sn-perovskite series.

In the B1 system, two distinct activation-energy regimes are observed from Arrhenius analysis of the photocurrent amplitude. At low temperatures, E_a = 0.13 ± 0.03 eV corresponds to the energy required to liberate mobile species from shallow defect states—primarily iodide vacancies weakly bound in the 2D lattice. Above a certain temperature (∼320 K), the photocurrent amplitude undergoes a pronounced increase in slope, yielding a much greater apparent E_a of 1.4 ± 0.05 eV. This sudden jump reflects the onset of a higher-energy process, most likely associated with the thermal activation of deeper interfacial traps or the breaking of stronger divalent-spacer-framework interactions that transiently "lock up" ions until sufficient thermal energy is available to release them. The elevated barrier in this high-temperature regime, therefore, signals the emergence of a secondary, more strongly bound defect population-mediated migration pathway that dominates ionic motion once the 2D framework begins to stiffen under continued heating.

In the E1 system, three activation-energy regimes emerge from the temperature-dependent photocurrent amplitude: approximately 0.34 ± 0.03 eV at low temperatures, 0.50 ± 0.03 eV in the midtemperature range, and rising further to 0.70 ± 0.04 eV at high temperatures. The sharp increase in activation energy at higher temperatures reflects deep-trap potentials and intensified electric fields from charged defect clusters and grain boundaries that "pin" mobile ions until sufficient thermal energy is available. The E1 network maintains a rigid, interconnected trap landscape. This rigidity enforces consistently high migration barriers that require substantial thermal input to enable ionic motion.

The E1B1 hybrid structure also exhibits a three-regime activation profile that reflects its mixed dimensionality and evolving interfacial landscape. In the low temperature regime, an E_a of 0.24 ± 0.03 eV indicates that the 2D cap layer effectively passivates surface defects and relaxes the underlying 3D lattice, facilitating ion migration across the interface with a reduced barrier height. As temperature increases into the midrange, E_a rises to 0.43 ± 0.03 eV, signaling the formation of thermally activated trap states at the 2D/3D boundary, likely due to ion accumulation and structural mismatch, that impede long-range vacancy diffusion. In the high temperature regime, E_a further escalates to 0.63 ± 0.04 eV, marking the dominance of deep interfacial traps and strengthened electrostatic pinning that substantially hinders ionic redistribution.

Comparing our Sn-based activation energies with those reported for Pb-halide analogues, we emerge several key insights. In 3D $MAPbI_3$, reported activation energies lie between 0.2 and 0.3 eV, consistent with iodide-vacancy migration.[40,42] In contrast, our $FASnI_3$ (E1) films exhibit a base-level barrier of 0.34 eV that rises to 0.50 eV and 0.70 eV at higher temperatures, pointing to increasingly deep trap states and stronger grain-boundary immobilization than in lead analogues. Notably, similar multistep activation energy behavior has also been observed in $MAPbI_3$ under certain bias and temperature conditions.[68] Likewise, both B1 and E1B1 start with low barriers (∼0.13 eV) reflecting facile vacancy release from shallow traps in well-passivated 2D lattices. However, as temperature rises, they switch into much higher-energy regimes (>0.4 eV, reaching ∼1.4 eV for B1), evidencing the thermal activation of deeper defect populations and interfacial traps unique to Sn perovskites with mixed oxidation states and strong spacer−framework interactions.

3.2. Mechanism. In lateral TPC measurements, the photocurrent rise time (τ_{rise}) and the stabilized photocurrent amplitude (I_{ph}) together offer direct mechanistic insight into the barriers and traps governing carrier extraction in Sn perovskites. In the 2D $BDASnI_4$ (B1) system, τ_{rise} is rapid (∼1.2 ms) because only shallow surface and interfacial states require filling before steady-state drift is established, and ionic screening is negligible due to the insulating organic spacers. However, I_{ph} is the lowest of the series: carriers are laterally confined to short diffusion lengths and must surmount

https://doi.org/10.1021/acs.jpcc.5c05203
J. Phys. Chem. C 2025, 129, 18563−18570

potential steps at each spacer layer, limiting the net extracted current.

In contrast, in the 3D $FASnI_3$ (E1) film, τ_{rise} slows dramatically (~90 ms) as photocarriers sequentially occupy abundant deep Sn-related traps; only after these defects fill and mobile iodide vacancies partially screen the bias field can efficient drift occur. Once this internal field builds, I_{ph} reaches its maximum since carriers would like to extend transport pathways across the continuous 3D network.

The physically paired E1B1 hybrid bridges these extremes: τ_{rise} (~88 ms) shortens relative to pure E1 because the 2D cap layer passivates interfacial traps and reduces the initial trap-filling burden, while I_{ph} remains substantially higher than B1, thanks to the 3D backbone's long-range transport and ionic field screening.

Across all compositions, raising temperature uniformly decreases τ_{rise} and increases I_{ph}, confirming that thermal activation lowers ionic migration barriers, accelerating field establishment, and enhancing carrier mobilities. In this way, the combined τ_{rise} and I_{ph} metric succinctly encodes how electronic trap densities, ionic dynamics, and interfacial engineering together dictate extraction kinetics and steady-state performance in Sn-based perovskites.

4. CONCLUSION

This study reveals how lattice dimensionality and interfacial design dictate the intertwined electronic and ionic dynamics in tin perovskites, as probed by transient photocurrent (TPC) and in situ photoluminescence (PL). In the purely 2D $BDASnI_4$ (B1), quantum-well confinement and insulating diammonium spacers virtually eliminate deep traps and block long-range vacancy transport, yielding a fast photocurrent rise (τ_{rise} ~ 1 ms). In contrast, the 3D $FASnI_3$ (E1) lattice hosts abundant midgap defects and high migration barriers, producing a sluggish rise (τ_{rise} ~ 90 ms). In the physically paired E1B1 hybrid, τ_{rise} decreases with increasing temperature up to ~ 326 K-reflecting 2Dcap-induced passivation and lattice relaxation that accelerate charge extraction and then increases modestly beyond 326 K as interfacial ion accumulation and strain generate new trap states before stabilizing. These temperature-dependent transitions demonstrate that the dimensional hybrid structure can either enhance or undermine performance, depending on thermal and electrostatic conditions. Achieving both rapid response and thermal stability in Sn perovskites therefore requires precise control over Sn-defect populations, interfacial strain, and trap landscapes through tailored spacer chemistry and interface engineering—paving the way toward robust lead-free optoelectronics.

■ ASSOCIATED CONTENT

Supporting Information

The Supporting Information is available free of charge at https://pubs.acs.org/doi/10.1021/acs.jpcc.5c05203.

Experimental materials and thin film fabrication and steady-state photophysical and structural characterization (PDF)

■ AUTHOR INFORMATION

Corresponding Author

Eric Wei-Guang Diau − *Department of Applied Chemistry and Institute of Molecular Science, National Yang Ming Chiao Tung University, Hsinchu 300093, Taiwan; Center for Emergent Functional Matter Science, National Yang Ming Chiao Tung University, Hsinchu 300093, Taiwan;* orcid.org/0000-0001-6113-5679; Email: diau@nycu.edu.tw

Authors

Ashank Seetharaman − *Department of Applied Chemistry and Institute of Molecular Science, National Yang Ming Chiao Tung University, Hsinchu 300093, Taiwan;* orcid.org/0000-0002-4417-8631

Sudhakar Narra − *Department of Applied Chemistry and Institute of Molecular Science, National Yang Ming Chiao Tung University, Hsinchu 300093, Taiwan; Center for Emergent Functional Matter Science, National Yang Ming Chiao Tung University, Hsinchu 300093, Taiwan;* orcid.org/0000-0003-4893-9204

Parameswaran Rajamanickam − *Department of Materials Science and Engineering, National Yang Ming Chiao Tung University, Hsinchu 300093, Taiwan;* orcid.org/0000-0001-9377-2963

Nobuhiro Ohta − *Department of Applied Chemistry and Institute of Molecular Science, National Yang Ming Chiao Tung University, Hsinchu 300093, Taiwan; Center for Emergent Functional Matter Science, National Yang Ming Chiao Tung University, Hsinchu 300093, Taiwan;* orcid.org/0000-0003-4255-6448

Complete contact information is available at: https://pubs.acs.org/10.1021/acs.jpcc.5c05203

Funding

This work is supported by National Science and Technology Council (Grant No. NSTC 113-2639-M-A49-001-ASP and NSTC 114-2639-M-A49-001-ASP) and Center for Emergent Functional Matter Science of National Yang Ming Chiao Tung University (NYCU) from the Featured Areas Research Center Program within the framework of the Higher Education Sprout Project by Taiwan Ministry of Education (MOE).

Notes

The authors declare no competing financial interest.

■ REFERENCES

(1) Lee, M. M.; Teuscher, J.; Miyasaka, T.; Murakami, T. N.; Snaith, H. J. Efficient Hybrid Solar Cells Based on Meso-Superstructured Organometal Halide Perovskites. *Science* **2012**, *338* (6107), 643−647.

(2) Stranks, S. D.; Eperon, G. E.; Grancini, G.; Menelaou, C.; Alcocer, M. J. P.; Leijtens, T.; Herz, L. M.; Petrozza, A.; Snaith, H. J. Electron-Hole Diffusion Lengths Exceeding 1 Micrometer in an Organometal Trihalide Perovskite Absorber. *Science* **2013**, *342* (6156), 341−344.

(3) Cahen, D.; Kronik, L.; Hodes, G. Are Defects in Lead-Halide Perovskites Healed, Tolerated, or Both? *ACS Energy Lett.* **2021**, *6* (11), 4108−4114.

(4) Ye, J.; Mondal, N.; Carwithen, B. P.; Zhang, Y.; Dai, L.; Fan, X.-B.; Mao, J.; Cui, Z.; Ghosh, P.; Otero-Martínez, C.; et al. Extending the defect tolerance of halide perovskite nanocrystals to hot carrier cooling dynamics. *Nat. Commun.* **2024**, *15* (1), 8120.

(5) Wang, S.; Tan, L.; Zhou, J.; Li, M.; Zhao, X.; Li, H.; Tress, W.; Ding, L.; Graetzel, M.; Yi, C. Over 24% efficient MA-free $Cs_xFA_{1-x}PbX_3$ perovskite solar cells. *Joule* **2022**, *6* (6), 1344−1356.

(6) Jeong, J.; Kim, M.; Seo, J.; Lu, H.; Ahlawat, P.; Mishra, A.; Yang, Y.; Hope, M. A.; Eickemeyer, F. T.; Kim, M.; et al. Pseudo-halide anion engineering for α-$FAPbI_3$ perovskite solar cells. *Nature* **2021**, *592* (7854), 381−385.

(7) Xu, R.; Pan, F.; Chen, J.; Li, J.; Yang, Y.; Sun, Y.; Zhu, X.; Li, P.; Cao, X.; Xi, J.; et al. Optimizing the Buried Interface in Flexible

Perovskite Solar Cells to Achieve Over 24% Efficiency and Long-Term Stability. *Adv. Mater.* **2024**, *36* (7), 2308039.
(8) Han, J.; Park, K.; Tan, S.; Vaynzof, Y.; Xue, J.; Diau, E. W.-G.; Bawendi, M. G.; Lee, J.-W.; Jeon, I.; et al. Perovskite solar cells. *Nat. Rev. Methods Primers* **2025**, *5* (1), 3.
(9) Jokar, E.; Chien, C.-H.; Fathi, A.; Rameez, M.; Chang, Y.-H.; Diau, E. W.-G. Slow surface passivation and crystal relaxation with additives to improve device performance and durability for tin-based perovskite solar cells. *Energy Environ. Sci.* **2018**, *11* (9), 2353−2362.
(10) Jokar, E.; Chien, C. -H.; Tsai, C. -M.; Fathi, A.; Diau, E. W. -G. Robust Tin-Based Perovskite Solar Cells with Hybrid Organic Cations to Attain Efficiency Approaching 10%. *Adv. Mater.* **2019**, *31* (2), 1804835.
(11) Hao, F.; Stoumpos, C. C.; Cao, D. H.; Chang, R. P. H.; Kanatzidis, M. G. Lead-free solid-state organic−inorganic halide perovskite solar cells. *Nat. Photonics* **2014**, *8* (6), 489−494.
(12) Rajamanickam, P.; Narra, S.; Seetharaman, A.; Diau, E. W.-G. Highly Efficient HTM-Free Tin Perovskite Solar Cells with Outstanding Stability Exceeding 10000 h. *ACS Appl. Mater. Interfaces* **2023**, *15* (34), 40700−40708.
(13) Zhang, M.; Wu, C.; Yin, M.; Yao, H.; Qiu, H.; Luo, J.; Du, J.; Hao, F. High Efficiency Tin Halide Perovskite Solar Cells with Over 1 Micrometer Carrier Diffusion Length. *Adv. Funct. Mater.* **2024**, *34* (52), 2410772.
(14) Zhu, Z.; Jiang, X.; Yu, D.; Yu, N.; Ning, Z.; Mi, Q. Smooth and Compact $FASnI_3$ Films for Lead-Free Perovskite Solar Cells with over 14% Efficiency. *ACS Energy Lett.* **2022**, *7* (6), 2079−2083.
(15) Stacchini, V.; Rastgoo, M.; Marčinskas, M.; Frasca, C.; Morita, K.; Frohloff, L.; Treglia, A.; Gries, T. W.; Karalis, O.; Getautis, V.; et al. Phenothiazine-Based Self-Assembled Monolayer with Thiophene Head Groups Minimizes Buried Interface Losses in Tin Perovskite Solar Cells. *Adv. Energy Mater.* **2025**, *15* (29), 2500841.
(16) Wang, L.; Bi, H.; Liu, J.; Wei, Y.; Zhang, Z.; Chen, M.; Baranwal, A. K.; Kapil, G.; Kitamura, T.; Yang, S.; et al. Exceeding 15% Performance with Energy Level Tuning in Tin-Based Perovskite Solar Cells. *ACS Energy Lett.* **2024**, *9* (12), 6238−6244.
(17) Gatto, L.; Poli, I.; Meggiolaro, D.; Grandi, F.; Folpini, G.; Treglia, A.; Cinquanta, E.; Petrozza, A.; Angelis, F. D.; Vozzi, C. Charge-Phonon Coupling in Tin Halide Perovskites. *ACS Energy Lett.* **2025**, *10* (3), 1382−1388.
(18) Gregori, L.; Frasca, C.; Meggiolaro, D.; Belanzoni, P.; Ashraf, M. W.; Musiienko, A.; Abate, A.; Angelis, F. D. Reducing p-Doping of Tin Halide Perovskites by Trivalent Cation Doping. *ACS Energy Lett.* **2024**, *9* (6), 3036−3041.
(19) Lanzetta, L.; Webb, T.; Zibouche, N.; Liang, X.; Ding, D.; Min, G.; Westbrook, R. J. E.; Gaggio, B.; Macdonald, T. J.; Islam, M. S.; et al. Degradation mechanism of hybrid tin-based perovskite solar cells and the critical role of tin (IV) iodide. *Nat.Commun.* **2021**, *12* (1), 2853.
(20) Ricciarelli, D.; Meggiolaro, D.; Ambrosio, F.; Angelis, F. D. Instability of Tin Iodide Perovskites: Bulk p-Doping versus Surface Tin Oxidation. *ACS Energy Lett.* **2020**, *5* (9), 2787−2795.
(21) Xu, Y.; Kim, J.; Ramakrishnan, S.; Chen, T.; Zhang, X.; Zhang, Y.; Musser, A. J.; Yu, Q. Unraveling the Formation Mechanisms of Highly Oriented Tin Perovskite with a 3D-over-2D Heterostructure. *ACS Energy Lett.* **2024**, *9* (9), 4734−4745.
(22) Zhao, J.; Zhang, Z.; Li, G.; Aldamasy, M. H.; Li, M.; Abate, A. Dimensional Tuning in Lead-Free Tin Halide Perovskite for Solar Cells. *Adv. Energy Mater.* **2023**, *13* (13), 2204233.
(23) Liao, Y.; Liu, H.; Zhou, W.; Yang, D.; Shang, Y.; Shi, Z.; Li, B.; Jiang, X.; Zhang, L.; Quan, L. N.; et al. Highly Oriented Low-Dimensional Tin Halide Perovskites with Enhanced Stability and Photovoltaic Performance. *J. Am. Chem. Soc.* **2017**, *139* (19), 6693−6699.
(24) He, D.; Chen, P.; Steele, J. A.; Wang, Z.; Xu, H.; Zhang, M.; Ding, S.; Zhang, C.; Lin, T.; Kremer, F.; et al. Homogeneous 2D/3D heterostructured tin halide perovskite photovoltaics. *Nat. Nanotechnol.* **2025**, *20* (6), 779−786.
(25) Feng, G.; Loi, H.-L.; Wang, T.; Deng, W.; Guan, Z.; Wei, Q.; He, J.; Li, M.; Lee, C.-S.; Wang, J.; et al. A-Site Engineering with Thiophene-Based Ammonium for High-Efficiency 2D/3D Tin Halide Perovskite Solar Cells. *Angew. Chem. Int. Ed.* **2025**, *64* (1), No. e202413584.
(26) Chang, B.; Wang, L.; Li, H.; Pan, L.; Wu, Y.; Liu, Z.; Zhang, Y.-N.; Guo, E.; Yin, L. Phase-Pure 2D/3D Tin-Based Perovskite Films for Solar Cells. *ACS Energy Lett.* **2024**, *9* (2), 363−372.
(27) Kang, Z.; Feng, P.; Wang, K.; Zhang, L.; Meng, R.; Chen, Y.; Wu, J.; Yang, F.; Zhang, X.; Li, T.; et al. Synchronous dimension-crystallization engineering enables highly efficient 2D/3D tin perovskite solar cells. *Energy Environ. Sci.* **2025**, *18* (9), 4108−4119.
(28) Yu, B.-B.; Chen, Z.; Zhu, Y.; Wang, Y.; Han, B.; Chen, G.; Zhang, X.; Du, Z.; He, Z. Heterogeneous 2D/3D Tin-Halides Perovskite Solar Cells with Certified Conversion Efficiency Breaking 14%. *Adv. Mater.* **2021**, *33* (36), 2102055.
(29) Chen, Y.; Wang, K.; Chen, W.; Li, T.; Tu, H.; Yang, F.; Kang, Z.; Tong, Y.; Wang, H. Defects Mitigation and Charge Transport Promotion via a Multifunctional Lewis Base for Efficient 2D/3D Tin Perovskite Solar Cells. *Adv. Energy Mater.* **2025**, *15* (22), 2406024.
(30) Du, F.; Gu, H.; Jiang, W.; Yang, W.; Lin, Y.; Zhu, W.; Qin, X.; Xie, X.; Bu, L.; Liu, X.; et al. Managing Crystallization and Phase Distribution via 2D Perovskite Seed Crystals for 2D-3D Tin-based Perovskite Solar Cells. *Adv. Funct. Mater.* **2025**, *35* (3), 2413281.
(31) Jokar, E.; Cheng, P.-Y.; Lin, C.-Y.; Narra, S.; Shahbazi, S.; Wei-Guang Diau, E. Enhanced Performance and Stability of 3D/2D Tin Perovskite Solar Cells Fabricated with a Sequential Solution Deposition. *ACS Energy Lett.* **2021**, *6* (2), 485−492.
(32) Seetharaman, A.; Narra, S.; Rajamanickam, P.; Putikam, R.; Lin, M.-C.; Wei-Guang Diau, E. Diffusion of bulky organic cations in the 3D/2D heterostructures to form interfacial quasi-2D (N2) phase for tin perovskite solar cells. *J. Mater. Chem. A* **2023**, *11* (39), 21089−21098.
(33) Mathew, P. S.; Kamat, P. V. Cation Migration in Physically Paired 2D and 3D Lead Halide Perovskite Films. *Adv. Opt. Mater.* **2024**, *12* (8), 2300957.
(34) Elmelund, T.; Scheidt, R. A.; Seger, B.; Kamat, P. V. Bidirectional Halide Ion Exchange in Paired Lead Halide Perovskite Films with Thermal Activation. *ACS Energy Lett.* **2019**, *4* (8), 1961−1969.
(35) Cho, J.; Dubose, J. T.; Le, A. N. T.; Kamat, P. V. Suppressed Halide Ion Migration in 2D Lead Halide Perovskites. *ACS Mater. Lett.* **2020**, *2* (6), 565−570.
(36) Jang, Y.-W.; Lee, S.; Yeom, K. M.; Jeong, K.; Choi, K.; Choi, M.; Noh, J. H. Intact 2D/3D halide junction perovskite solar cells via solid-phase in-plane growth. *Nat. Energy* **2021**, *6* (1), 63−71.
(37) Calado, P.; Telford, A. M.; Bryant, D.; Li, X.; Nelson, J.; O'Regan, B. C.; Barnes, P. R. F. Evidence for ion migration in hybrid perovskite solar cells with minimal hysteresis. *Nat. Commun.* **2016**, *7* (1), 13831.
(38) Zhang, T.; Chen, H.; Bai, Y.; Xiao, S.; Zhu, L.; Hu, C.; Xue, Q.; Yang, S. Understanding the relationship between ion migration and the anomalous hysteresis in high-efficiency perovskite solar cells: A fresh perspective from halide substitution. *Nano Energy* **2016**, *26*, 620−630.
(39) Belisle, R.A.; Nguyen, W.H.; Bowring, A.R.; Calado, P.; Li, X.; Irvine, S. J.; McGehee, M. D.; Barnes, P. R. F; O'Regan, B. C.; et al. Interpretation of inverted photocurrent transients in organic lead halide perovskite solar cells: proof of the field screening by mobile ions and determination of the space charge layer widths. *Energy Environ. Sci.* **2017**, *10* (1), 192−204.
(40) Ni, Z.; Jiao, H.; Fei, C.; Gu, H.; Xu, S.; Yu, Z.; Yang, G.; Deng, Y.; Jiang, Q.; Liu, Y.; et al. Evolution of defects during the degradation of metal halide perovskite solar cells under reverse bias and illumination. *Nat. Energy* **2022**, *7* (1), 65−73.
(41) Reichert, S.; An, Q.; Woo, Y.-W.; Walsh, A.; Vaynzof, Y.; Deibel, C. Probing the ionic defect landscape in halide perovskite solar cells. *Nat. Commun.* **2020**, *11* (1), 6098.

https://doi.org/10.1021/acs.jpcc.5c05203
J. Phys. Chem. C 2025, 129, 18563−18570

(42) Schmidt, M. C.; Alvarez, A. O.; Boer, J. J. D.; Ven, L. J. M. V. D.; Ehrler, B. Consistent Interpretation of Time- and Frequency-Domain Traces of Ion Migration in Perovskite Semiconductors. *ACS Energy Lett.* **2024**, *9* (12), 5850−5858.
(43) Baier, N.; Brambilla, A.; Feuillet, G.; Renet, S. Photo-induced current transient spectroscopy studies on polycrystalline CdTe. *Nucl. Instrum. Methods Phys. Res., Sect. A* **2006**, *563* (1), 155−158.
(44) Mathew, X. Photo-induced current transient spectroscopic study of the traps in CdTe. *Sol. Energy Mater. Sol. Cells* **2003**, *76* (3), 225−242.
(45) Bisquert, J.; Gonzales, C.; Guerrero, A. Transient On/Off Photocurrent Response of Halide Perovskite Photodetectors. *J. Phys. Chem. C* **2023**, *127* (43), 21338−21350.
(46) Armaroli, G.; Maserati, L.; Ciavatti, A.; Vecchi, P.; Piccioni, A.; Foschi, M.; Meer, V. V. D.; Cortese, C.; Feldman, M.; Foderà, V.; et al. Photoinduced Current Transient Spectroscopy on Metal Halide Perovskites: Electron Trapping and Ion Drift. *ACS Energy Lett.* **2023**, *8* (10), 4371−4379.
(47) Pecunia, V.; Zhao, J.; Kim, C.; Tuttle, B. R.; Mei, J.; Li, F.; Peng, Y.; Huq, T. N.; Hoye, R. L. Z.; Kelly, N. D.; et al. Assessing the Impact of Defects on Lead-Free Perovskite-Inspired Photovoltaics via Photoinduced Current Transient Spectroscopy. *Adv. Energy Mater.* **2021**, *11* (22), 2003968.
(48) Ciavatti, A.; Foderà, V.; Armaroli, G.; Maserati, L.; Colantoni, E.; Fraboni, B.; Cavalcoli, D. Radiation Hardness and Defects Activity in PEA_2PbBr_4 Single Crystals. *Adv. Funct. Mater.* **2024**, *34* (46), 2405291.
(49) Gordillo, G.; Otálora, C. A.; Ramirez, A. A. A study of trap and recombination centers in $MAPbI_3$ perovskites. *Phys. Chem. Chem. Phys.* **2016**, *18* (48), 32862−32867.
(50) Ghosh, S.; Paul, S.; De, S. K. Control Synthesis of Air-Stable Morphology Tunable Pb-Free Cs_2SnI6 Perovskite Nanoparticles and Their Photodetection Properties. *Part. Part. Syst. Charact* **2018**, *35* (9), 1800199.
(51) Lin, Z.; Lin, Z.; Wu, H.; Huang, R.; Song, J.; Chen, K.; Xia, L.; Zhang, Y.; Lin, H.; Li, H.; et al. Plasma-Enhanced Grain Growth and Non-Radiative Recombination Mitigation in CsSnBr3 Perovskite Films for High-Performance, Lead-Free Photodetectors. *Small* **2025**, *21* (6), 2411086.
(52) Yin, Q.; Wu, J.; Ye, H.; Li, H.; Zhu, Z.-K.; Zhang, C.; Xu, L.; Han, Z.; Luo, J. Environmental-Friendly Self-Powered Polarization Photodetector Based on Lead-Free Halide Double Perovskite Single Crystals with Asymmetric Contacts. *Adv. Opt. Mater.* **2025**, *13* (16), 2403183.
(53) Zhang, Y.; Ma, Y.; Wang, Y.; Zhang, X.; Zuo, C.; Shen, L.; Ding, L. Lead-Free Perovskite Photodetectors: Progress, Challenges, and Opportunities. *Adv. Mater.* **2021**, *33* (26), 2006691.
(54) Mandal, A.; Khuntia, S. K.; Mondal, D.; Mahadevan, P.; Bhattacharyya, S. Spin Texture Sensitive Photodetection by Dion−Jacobson Tin Halide Perovskites. *J. Am. Chem. Soc.* **2023**, *145*, 24990−25002.
(55) Wang, H.; Yin, Y.; Xu, J.; Li, J.; Bao, Y.; An, M.; Tang, L.; Jin, S.; Tian, W.; Yang, Y. Field-Induced Transport Anisotropy in Single-Crystalline All-Inorganic Lead-Halide Perovskite Nanowires. *ACS Nano* **2023**, *17* (23), 23671−23678.
(56) Ji, H.; Liu, X.; Li, L.; Zhang, F.; Qin, L.; Lou, Z.; Li, D.; Hu, Y.; Hou, Y.; Teng, F. Two-dimensional layered Dion−Jacobson phase organic−inorganic tin iodide perovskite field-effect transistors. *J. Mater. Chem. A* **2023**, *11* (14), 7767−7779.
(57) Park, W.; Kwon, M.; Lee, D. H.; Yoo, S.; Yang, W.; Park, J.-S.; Liu, A.; Reo, Y.; Zhu, H.; Noh, Y.-Y. Odd−Even Effects of Linear Alkyl-Based Organic Spacers for Efficient Charge Transport in Two-Dimensional Dion−Jacobson Tin Perovskites. *J. Am. Chem. Soc.* **2025**, *147* (21), 17926−17935.
(58) Li, L.; Jia, P.; Bi, W.; Tang, Y.; Song, B.; Qin, L.; Lou, Z.; Hu, Y.; Teng, F.; Hou, Y. Impacts of carrier trapping and ion migration on charge transport of perovskite solar cells with TiOx electron transport layer. *RSC Adv.* **2020**, *10* (47), 28083−28089.
(59) Futscher, M. H.; Deibel, C. Defect Spectroscopy in Halide Perovskites Is Dominated by Ionic Rather than Electronic Defects. *ACS Energy Lett.* **2022**, *7* (1), 140−144.
(60) Basumatary, P.; Agarwal, P. Photocurrent transient measurements in $MAPbI_3$ thin films. *J. Mater. Sci.:Mater. Electron.* **2020**, *31* (13), 10047−10054.
(61) Cho, Y.; Jung, H. R.; Jo, W. Photo-induced defects in $MAPbBr_3$ single crystals. *J. Phys. Energy* **2021**, *3* (4), 044005.
(62) Kober-Czerny, M.; Motti, S. G.; Holzhey, P.; Wenger, B.; Lim, J.; Herz, L. M.; Snaith, H. J. Excellent Long-Range Charge-Carrier Mobility in 2D Perovskites. *Adv. Funct. Mater.* **2022**, *32* (36), 2203064.
(63) Liu, Y.; Zheng, X.; Fang, Y.; Zhou, Y.; Ni, Z.; Xiao, X.; Chen, S.; Huang, J.; Liu, Y.; Zheng, X.; et al. Ligand assisted growth of perovskite single crystals with low defect density. *Nat. Commun.* **2021**, *12* (1), 1686.
(64) Milot, R. L.; Eperon, G. E.; Snaith, H. J.; Johnston, M. B.; Herz, L. M. Temperature-Dependent Charge-Carrier Dynamics in $CH_3NH_3PbI_3$ Perovskite Thin Films. *Adv. Funct. Mater.* **2015**, *25* (39), 6218−6227.
(65) Zhang, T.; Zhou, C.; Feng, X.; Dong, N.; Chen, H.; Chen, X.; Zhang, L.; Lin, J.; Wang, J.; et al. Regulation of the luminescence mechanism of two-dimensional tin halide perovskites. *Nat. Commun.* **2022**, *13* (1), 60.
(66) Fasahat, S.; Fiuza-Maneiro, N.; Schäfer, B.; Xu, K.; Gómez-Graña, S.; Alonso, M. I.; Polavarapu, L.; Goñi, A. R. Sign of the Gap Temperature Dependence in $CsPb(Br,Cl)_3$ Nanocrystals Determined by Cs-Rattler-Mediated Electron−Phonon Coupling. *J. Phys. Chem. Lett.* **2025**, *16* (4), 1134−1141.
(67) Wang, S.; Ma, J.; Li, W.; Wang, J.; Wang, H.; Shen, H.; Li, J.; Wang, J.; Luo, H.; Li, D. Temperature-Dependent Band Gap in Two-Dimensional Perovskites: Thermal Expansion Interaction and Electron−Phonon Interaction. *J. Phys. Chem. Lett.* **2019**, *10* (10), 2546−2553.
(68) Zhao, Y.-C.; Zhou, W.-K.; Zhou, X.; Liu, K.-H.; Yu, D.-P.; Zhao, Q. Quantification of light-enhanced ionic transport in lead iodide perovskite thin films and its solar cell applications. *Light: Sci. Appl.* **2016**, *6* (5), No. e16243.

https://doi.org/10.1021/acs.jpcc.5c05203
J. Phys. Chem. C 2025, 129, 18563−18570